Published in final edited form as:
J Magn Reson. 2010 June ; 204(2): 303–313. doi:10.1016/j.jmr.2010.03.016.

Low-Temperature Dynamic Nuclear Polarization at 9.4 Tesla With a 30 Milliwatt Microwave Source

Kent R. Thurber, **Wai-Ming Yau**, and **Robert Tycko***
Laboratory of Chemical Physics, National Institute of Diabetes and Digestive and Kidney Diseases, National Institutes of Health, Bethesda, MD 20892-0520

Abstract

Dynamic nuclear polarization (DNP) can provide large signal enhancements in nuclear magnetic resonance (NMR) by transfer of polarization from electron spins to nuclear spins. We discuss several aspects of DNP experiments at 9.4 Tesla (400 MHz resonant frequency for ^{1}H, 264 GHz for electron spins in organic radicals) in the 7–80 K temperature range, using a 30 mW, frequency-tunable microwave source and a quasi-optical microwave bridge for polarization control and low-loss microwave transmission. In experiments on frozen glycerol/water doped with nitroxide radicals, DNP signal enhancements up to a factor of 80 are observed (relative to ^{1}H NMR signals with thermal equilibrium spin polarization). The largest sensitivity enhancements are observed with a new triradical dopant, DOTOPA-TEMPO. Field modulation with a 10 G root-mean-squared amplitude during DNP increases the nuclear spin polarizations by up to 135%. Dependencies of ^{1}H NMR signal amplitudes, nuclear spin relaxation times, and DNP build-up times on the dopant and its concentration, temperature, microwave power, and modulation frequency are reported and discussed. The benefits of low-temperature DNP can be dramatic: the ^{1}H spin polarization is increased approximately 1000-fold at 7 K with DNP, relative to thermal polarization at 80 K.

Keywords

solid state nuclear magnetic resonance; sensitivity enhancement; hyperpolarization; nitroxide; TEMPO; spin-lattice relaxation; paramagnetic relaxation

1. Introduction

Dynamic nuclear polarization (DNP) is a powerful method to increase nuclear spin polarizations by transferring polarization from unpaired electron spins. Because the electron spin energy splitting is 660 times greater than that of ^{1}H nuclei, ^{1}H nuclear spin polarizations can be increased by more than a factor of 100. Similar enhancements of nuclear magnetic resonance (NMR) signals are then observed. Since the time required for an NMR experiment limited by random noise depends on the square of the signal-to-noise, a signal increase by a factor of 100 reduces the experiment time by a factor of 10,000, all other things being equal. This time reduction enables experiments that would be impractical otherwise.

*corresponding author: Dr. Robert Tycko, National Institutes of Health, Building 5, Room 112, Bethesda, MD 20892-0520; phone 301-402-8272; fax 301-496-0825; robertty@mail.nih.gov.

DNP was predicted in 1953 by Overhauser [1], and seen experimentally in the same year by Carver and Slichter [2]. Since then, many techniques have been discovered for transferring polarization from electron spins to nuclear spins. For examples, see recent DNP reviews [3, 4]. In this article, we focus on the relatively simple technique of DNP driven by continuous microwave irradiation of electron paramagnetic resonance (EPR) lines. For applications in solid state NMR of organic and biochemical systems, related experiments were performed in the 1980s and 1990s by Wind et al.[5], Singel et al.[6], and Afeworki et al.[7] at magnetic fields of 1.4 T (40 GHz microwave frequency). DNP experiments at higher fields have been pioneered by Griffin and coworkers, using gyrotron microwave sources capable of providing many watts of microwave power at frequencies of 140 GHz and above [8–11]. High-frequency diode-multiplierbased sources have also become commercially available, physically smaller and less expensive than a gyrotron, with power outputs in the 10–100 mW range. Such sources have also been used for DNP at 140 GHz [12–16].

DNP mechanisms generally become weaker at higher fields [3], suggesting that high-field DNP experiments might not be successful. However, Griffin and coworkers have shown that large solid state NMR signal enhancements are readily obtained with the aid of biradical dopants that improve DNP efficiencies by providing electron spins in coupled pairs [17–19]. Coupled electron spins are crucial for several DNP mechanisms. For the cross effect, an inhomogeneously broadened EPR line is required, with two electrons whose resonance frequencies are separated by the NMR frequency [18,20,21]. This allows an energy-conserving three-spin process in which the two electrons exchange spin states, with the energy difference between them provided by a simultaneous nuclear spin flip (which tends to polarize nuclear spins when the two electrons have different initial polarizations). For a homogeneously broadened EPR line, with a linewidth greater than the NMR frequency, the DNP process is described as thermal mixing [5]. Off-center irradiation of the EPR line creates a polarization of the electron dipolar system, which can then be transferred to the nuclei. Recent developments in microwave sources and biradical dopants has led to renewed interest in high-field DNP for NMR spectroscopy [22–30].

In this paper, we report the results of DNP experiments at 9.4 T using a compact and relatively inexpensive (but relatively low-power) solid state microwave source, in which we observe ^{1}H NMR signals from frozen glycerol/water solutions that are doped with several nitroxide radical compounds. Glycerol/water solutions are of particular interest because of their relevance to our studies of proteins and protein complexes in frozen solutions [31–37]. We present data regarding the dependencies of ^{1}H NMR signals, nuclear spin relaxation times, and DNP build-up times on dopant, dopant concentration, temperature (7–80 K range), and microwave power. We introduce a new triradical dopant, DOTOPA-TEMPO, that produces the largest sensitivity enhancements in our experiments. We also show that DNP enhancements can be increased substantially by application of magnetic field modulation during microwave irradiation, and we discuss possible mechanisms for this effect. The primary conclusion of this work is that quite large enhancements of NMR sensitivity can be achieved in high fields with relatively low microwave powers, provided that low temperatures are also employed. Relative to signals at 80 K with thermal equilibrium nuclear spin polarization and taking into account the temperature-dependence of the DNP build-up time, the sensitivity of ^{1}H NMR measurements is increased by factors greater than 10, 50, 180, and 400 at 80 K, 35 K, 16 K, and 7 K, respectively, in our experiments with 30 mM DOTOPA-TEMPO as the dopant.

2. Materials and Methods

2.1 Nitroxide dopants

4-amino-TEMPO and 4-hydroxy-TEMPO were used as purchased from Sigma-Aldrich. The biradical TOTAPOL and the triradical DOTOPA-TEMPO (4-[N,N-di-(2-hydroxy-3-

(TEMPO-4'-oxy)-propyl)]-amino-TEMPO) were synthesized based on the procedure given in Song, et al. for TOTAPOL [17]. Chemical structures are shown in Figure 1. The synthesis was modified by reacting 4-amino-TEMPO and 4-(2,3-epoxypropoxy)-TEMPO in 1:1.7 ratio, rather than a 1:1 ratio. Both the biradical and triradical were purified from the same synthesis by chromatography. ESI TOF mass spectrometry indicated a mass of 628.49 Da for the triradical, in good agreement with the proposed structure ($C_{33}H_{63}N_4O_7$, theoretical average mass = 627.87 Da). For TOTAPOL ($C_{21}H_{41}N_3O_4$, theoretical average mass = 399.57 Da), the measured mass was 400.32 Da.

Differences in the electron-electron interactions for the biradical and the triradical are clearly seen in the low-field (10 GHz) EPR spectra for 4-hydroxy-TEMPO, TOTAPOL, and DOTOPA-TEMPO shown in Figure 1. The low-field EPR spectra in solution are dominated by hyperfine interactions with ^{14}N nuclei. 4-hydroxy-TEMPO shows the three lines corresponding to the three spin states of a single ^{14}N nucleus. If electrons exchange among the nitroxide sites within a single molecule, the EPR lines of the biradical and triradical reflect an average over the multiple ^{14}N sites. In the fast-exchange limit, this results in five EPR lines for the biradical (total z-component of ^{14}N spin from −2 to +2) and seven EPR lines for the triradical (total z-component of ^{14}N spin from −3 to +3) [38,39]. Although the EPR spectrum of the triradical is not fully resolved, seven peaks in the derivative spectrum are seen (Figure 1c). Strong features in the derivative spectrum at the edges and in the center are characteristic of exchange-broadened spectra [18,38,40], as EPR lines that correspond to ^{14}N spin states that are the same on all nitroxide moieties (*i.e.*, the |+1,+1,+1>, |0,0,0>, and |−1,−1,−1> nuclear spin states) remain sharp in the presence of exchange. These lines occur at the same positions as the hyperfine-split lines of 4-hydroxy-TEMPO (Figure 1a). Similarly, the EPR spectrum of TOTAPOL shows three sharp lines of equal intensity and broad, unresolved features between these lines (Figure 1b). This is consistent with narrow EPR lines for the |+1,+1>, |0,0>, and |−1,−1> ^{14}N spin states and broad lines for other ^{14}N spin states [18].

Nitroxide concentrations were verified by titration with ascorbic acid [41], monitored by the UV-visible absorption spectrum. The UV-visible spectrum has a strong absorbance below 300 nm and a weak absorbance at longer wavelength (peaked at 435 nm for DOTOPA-TEMPO) that produces a yellow-orange color, both in the solid form and in solution. Reduction with ascorbic acid attenuates the 435 nm absorption (see Figure S1 of Supplementary Material). Based on titration of the 435 nm absorption, our DOTOPA-TEMPO had 109 ± 15% of the expected radical concentration (measured at 20 mM in 25/75 mol% glycerol/water). The titration procedure was validated on commercial 4-hydroxy-TEMPO (75 mM in glycerol/water). For TOTAPOL, we measured 85 ± 15% of the expected radical concentration (45 mM in water). Solutions of these nitroxides in glycerol/water were found to degrade over periods of many days, especially at high concentrations, as indicated by a weakening of the yellow-orange color. Therefore, fresh solutions were prepared for each set of experiments. Sample volumes in DNP experiments were 10 μl, with nitroxide concentrations between 20 mM and 320 mM in 25/75 mol% glycerol/water.

2.2 Quasi-optical microwave system and cryostat

Figure 2a shows the major components of our microwave system. The microwave source (1) from Virginia Diodes, Inc. (VDI; Charlottesville, Virginia; see http://www.virginiadiodes.com/) operates by multiplication of an 11 GHz signal up to the output frequency of 264 GHz, providing 30 mW of microwave power with an approximately 10 GHz tuning range. Frequency tunability is necessary because all experiments described below were performed in a conventional wide-bore 9.4 T superconducting NMR magnet, without a magnetic field sweep coil. The VDI source is compact, simple to operate, and allows electronic switching and attenuation of the microwave output power. It operates in the 100

Gauss fringe field of our NMR magnet, with magnetic shielding of the fundamental 11 GHz synthesizer and the cooling fan. We have used the source for approximately 200 hr to date, with no degradation of its performance. Unless otherwise noted, all DNP experiments were performed with the maximum microwave power from the VDI source (30 mW specified by VDI). The power output can be controlled by an external analog voltage, and the VDI source can be gated by an external TTL signal.

From the source, microwaves are transmitted through a quasi-optical system built by Thomas Keating, Ltd (West Sussex, United Kingdom; http://www.terahertz.co.uk/). After passing through a corrugated horn (gold colored in Figure 2a) that transfers the fundamental mode of the rectangular waveguide of the VDI source to a Gaussian beam [42], the microwaves pass through a wire grid polarizer (2), and then to a Martin-Puplett interferometer (3) [43]. The interferometer allows polarization control by splitting the microwave beam into two beams with orthogonal linear polarizations, which are then recombined after a variable path length, set with a micrometer adjustment. Polarization control allows us to put all of the microwave power into the circular polarization that is absorbed by the electron spins (see below), thereby maximizing DNP effects. After polarization, a mirror (4) reflects the microwave beam into a corrugated waveguide [44] that enters the NMR magnet from below and transmits the beam vertically to the cryostat within the magnet bore. The waveguide has an inner diameter of 13 mm. A corrugated horn at the end of the waveguide reduces the beam diameter to 2.5 mm before it enters the cryostat.

The head of the DNP/NMR cryostat is shown in Figure 2b. The cryostat is a customized Janis SuperTran continuous flow cryostat (similar to Janis model ST-200-NMR), in which the sample is thermally sunk to a temperature-controlled copper block (7), which is cooled by liquid helium, contained within a vacuum can, and surrounded by a radiation shield. The cryostat is inserted into the bore of the NMR magnet from above. The microwave beam crosses a high density polyethylene window (0.7 mm thick) at the bottom of the cryostat, crosses a short vacuum gap (0.8 mm), and enters a brass tube (6, 30 mm long, 3.2 mm inner diameter, 4.8 mm outer diameter) that carries the beam through the radiation shield (not shown in Figure 2) to the sample. The radio-frequency (RF) coil and sample sit just above the brass tube, with a 1.0 mm gap for electrical isolation.

The sample is contained in a Teflon cup (2.0 mm inner diameter, 3.2 mm outer diameter, 11 mm long). Microwaves pass through the bottom of the Teflon cup (~0.7 mm thick) to reach the sample. The sample is in contact with a sapphire rod (4 mm long) that inserts into the Teflon cup and is in contact with a copper cold finger, attached to the temperature-controlled copper block. All temperatures specified below are temperatures at the copper block, detected with an embedded Cernox sensor and controlled by a Lake Shore model 340 controller. Actual sample temperatures may be somewhat higher, especially during microwave irradiation at the lowest temperatures as discussed below. The sample is vacuum-sealed by a tight fit of the Teflon cup around the copper cold finger cylinder, with vacuum grease between Teflon and copper and an outer brass ring to prevent expansion of the Teflon. The RF coil is a two-turn Helmholtz coil, machined from a copper cylinder (7 mm long, 3.3 mm inner diameter, 6.4 mm outer diameter). Microwaves enter the RF coil through the bottom of the Helmholtz coil, with their propagation direction parallel to static magnetic field direction (*i.e.*, perpendicular to the RF magnetic field direction). The RF circuit is tuned and matched for ^{1}H NMR at 400.9 MHz, using a modified Polyflon variable capacitor for tuning and a ceramic chip capacitor for matching. The tuning capacitor is mounted on the same plate as the radiation shield. The RF coil and sample are surrounded by a field modulation coil (8), used for lock-in detection of EPR signals and for enhancement of DNP, as described below.

To minimize background ^{1}H NMR signals, the field modulation coil support and the support for the brass tube were made from Kel-F plastic. Remaining background signals are primarily from the insulation and epoxy cement on the modulation coil wire.

EPR lineshapes can be measured by the absorption of microwaves by the sample. After passing through the sample, a fraction of the remaining microwave beam passes through the sapphire rod, is reflected by the copper cold finger, passes through the sample again, and returns to the microwave quasi-optics through the corrugated waveguide. If the interferometric polarizer is set to produce circular polarization, the returning circularly polarized microwaves are reflected from the wire grid polarizer (2) into the EPR detector (5). Thus, the micrometer settings that produces circular polarization (right- or left-handed) can be determined by maximizing the reflected microwave power at the detector. The correct sense of circular polarization produces a maximum in the EPR signals, while the incorrect sense produces a null. The EPR detector consists of a corrugated horn that transfers the Gaussian beam into the fundamental mode of the rectangular waveguide of a diode detector (Pacific Millimeter Products). A lock-in amplifier (EG&G model 7220) provides a sinusoidal reference voltage (typically at 6100 Hz), which is amplified (Kepco model BOP 20–20M) to provide alternating current to the modulation coil (8), producing an oscillating field of several Gauss parallel to the main field of the superconducting magnet. The lock-in amplifier measures the sinusoidally modulated output of the diode detector, which is proportional to the derivative of the microwave absorption. For EPR measurements, the lock-in amplifier and VDI source frequency are controlled by a LabView program that steps the microwave frequency across the EPR line and stores the phase-sensitive lock-in outputs at each frequency.

We emphasize that our microwave system is designed primarily for DNP, not for EPR. Because the quasi-optical system has low attenuation and does not remove reflected microwave power, different microwave frequencies have different interference patterns from multiple reflections within the system. This produces periodic variations in the microwave power at the EPR detector as a function of frequency and causes oscillatory artifacts in the measured absorption derivatives in EPR spectra. Nonetheless, our system is adequate for measuring EPR lineshapes for comparison with the dependence of DNP effects on microwave frequency (as in Figure 4). EPR detection also enables an estimate of the fraction of microwave power that passes through the sample and returns to the detector. The measured EPR signal amplitude from a sample within the NMR cryostat is approximately 25% of the EPR signal amplitude from the same sample (solid 4-amino-TEMPO at room temperature) mounted directly at the end of the corrugated horn. This suggests that at least half (and probably significantly more than half) of the source power reaches the sample within the cryostat. This estimate is based on the fact that our EPR signals are detected as the loss of microwave power (due to resonant absorption by the sample) that reflects from the copper cold finger above the sample. If a fraction f_1 of the source power reached the sample and a fraction f_2 of the power that passes through the sample was reflected back to the corrugated waveguide, the EPR signals would be reduced by the factor $f_1 f_2$. Due to the geometry of our cryostat and sample holder, we expect $f_2 < f_1$.

2.3 Measurements of DNP enhancements

NMR measurements used a Varian Infinity spectrometer console. DNP-enhanced ^{1}H NMR signals at the lower temperatures were so large that a 6–40 db attenuator was placed before the RF receiver to prevent saturation of the preamplifier. For measurements of the effect of field modulation on DNP, an auxiliary output of the NMR pulse programmer was used to gate a sine wave from a waveform generator (Wavetek model 395), which was amplified to drive the modulation coil within the cryostat. The magnetic field produced by the modulation coil was calibrated as 5.0 G/A by measuring the frequency shift of liquid state ^{1}H NMR at room temperature as a function of current.

All solid state ^{1}H NMR signals were acquired with the RF pulse sequence in Figure 3a. After a train of 90° pulses to destroy ^{1}H spin polarization, the polarization recovered towards thermal equilibrium (without microwave irradiation) or towards its DNP-enhanced value (with microwave irradiation) during the delay τ. ^{1}H NMR signals were acquired after a pair of 90° pulses, *i.e.*, a solid echo sequence. A 180° pulse before the solid echo on alternating scans, with alternating addition and subtraction of the echo signals, helped suppress background signals. The background signal was measured as a function of temperature, and is subtracted from the measurements discussed below. For example, the background signal was 11% of the total signal without DNP at 16 K for 10 μl of 30mM DOTOPA-TEMPO, increasing to 28% at 80 K. Compared to signals with DNP, background signals were negligible. ^{1}H RF fields were in the 30–40 kHz range. In DNP measurements, the microwaves were applied continuously, without gating. Four scans with the RF phase cycle shown in Figure 3a were used in most measurements.

^{1}H NMR signal amplitudes, proportional to ^{1}H spin polarizations, were determined by integrating solid echo signals in the time domain, from 0 to 50 μs. DNP enhancements can in principle be reported relative to thermal equilibrium spin polarizations at some fixed sample temperature (*e.g.*, 300 K) or relative to thermal equilibrium spin polarizations at the sample temperature at which the DNP experiments are actually performed. We define the enhancement ξ_T to be the ratio of the ^{1}H NMR signal amplitude with DNP at sample temperature T to the equilibrium ^{1}H NMR signal amplitude (without DNP) at sample temperature T.

The DNP build-up time T_{DNP} was determined by fitting the integrated echo signals to the form $S(\tau)=S_0(1-e^{-\tau/T_{dnp}})$. When the signal-to-noise of an NMR measurement is limited by random noise that is independent of signal amplitudes, as is usually the case, the signal-to-noise achievable within a fixed experiment time is proportional to $S_0T_{DNP}^{-1/2}$. Therefore, we investigated both the DNP signal enhancements and the DNP build-up times in order to assess the sensitivity enhancements that could be obtained under various experimental conditions. Without microwaves, the same procedure was used to determine the ^{1}H spin-lattice relaxation time T_{1n}, including a constant offset to account for background signals or incomplete saturation.

Additional effects on NMR sensitivity due to temperature dependence of the quality factor Q of the RF circuitry and thermal noise reduction at lower temperatures are negligible in our experiments. The Q of the RF circuit within our cryostat increases by only 15% as the sample temperature decreases from 80 K to 16 K, because only the sample itself (and not the RF capacitors or coil) is cooled to the indicated temperatures.

3. Results

3.1 DNP signal enhancements and build-up times

Figure 3b compares ^{1}H NMR solid echo signals from glycerol/water with and without microwave irradiation at 11 K, using 30 mM DOTOPA-TEMPO and a 264.0 GHz microwave frequency. A dramatic signal enhancement is observed. Figure 4 compares the frequency dependencies of DNP enhancements under various experimental conditions with the EPR lineshape for 4-amino-TEMPO in frozen glycerol/water. As previously reported [12,21], the DNP enhancement is positive on the low-frequency side of the EPR line and negative on the high-frequency side, consistent with a three-spin cross effect mechanism [18,21]. Nitroxide radicals have the property that the width of their EPR lines in frozen solutions is comparable to the ^{1}H NMR frequency, facilitating the cross effect. For all dopants, the maximum enhancement is observed around 264.0 GHz, and this microwave frequency was used in all experiments described below. In our experiments, the largest enhancements are observed with DOTOPA-TEMPO, possibly because tethering of three nitroxide moieties (rather than one or

two) increases the probability that two nearby (and hence dipole-coupled) electron spins will have EPR frequencies that differ by the ^{1}H NMR frequency, due to differences in their g-anisotropy tensor orientations.

Figure 5 compares DNP build-up curves with ^{1}H saturation-recovery curves for glycerol/water doped with 4-amino-TEMPO under two different conditions. In both cases, T_{DNP} is similar to T_{1n}. This behavior is expected if the dominant longitudinal relaxation mechanism for ^{1}H spins is the same as the DNP mechanism, *i.e*., if both mechanisms involve the same nucleus-electron couplings and electron-electron couplings and the same spin transitions [45]. Differences between T_{DNP} and T_{1n} may arise from sample heating during microwave irradiation. T_{DNP} is an important parameter for practical applications of DNP, because the NMR signal-to-noise enhancement in a given experiment time (*i.e*., the real *sensitivity enhancement*) is proportional to both the asymptotic value of the ^{1}H spin polarization and the square root of T_{DNP}. Large polarizations that build up very slowly do not necessarily improve sensitivity, compared with smaller polarizations that build up quickly.

Table 1 summarizes measurements of DNP signal enhancements, build-up times, and sensitivity enhancements at several temperatures and various dopant conditions. Several aspects of these data are worth noting: (i) At very high dopant concentrations, such as 160 mM and 320 mM 4-amino-TEMPO, ^{1}H NMR signal amplitudes decrease significantly, presumably due to large paramagnetic shifts of NMR signals from ^{1}H nuclei that are close to the unpaired electron spins. Dipolar hyperfine shifts up to 200 kHz are expected at an electron-^{1}H distance of 0.9 nm. At 100 mM electron concentration, the fraction of the sample volume that lies within a 0.9 nm radius from an electron is roughly 20%. Even at lower dopant concentrations, such as 30 mM DOTOPA-TEMPO, signal losses attributed to paramagnetic shifts are not negligible, so that larger values of ξ_T do not necessarily translate directly into larger ^{1}H NMR signals; (ii) Biradical and triradical dopants produce both larger DNP-enhanced signals and shorter build-up times, relative to 4-amino-TEMPO. The sensitivity enhancement at a given temperature (*i.e*., the quantity $\xi_T \times T_{DNP}^{-1/2}$) can be more strongly affected by the reduction in T_{DNP}, at similar total electron spin concentrations; (iii) Although T_{DNP} increases with decreasing temperature, the DNP sensitivity enhancement still improves at lower temperatures because of the larger ξ_T values; (iv) When normalized to thermal equilibrium signals at 80 K, the DNP-enhanced signals at lower temperatures are enormous. For example, signals with 30 mM DOTOPA-TEMPO are larger than thermal equilibrium signals at 80 K by factors of roughly 70, 350, and 1000 at 35 K, 16 K, and 7 K, respectively. *Sensitivity* enhancements relative to measurements at 80 K without DNP may not be as large (depending on the paramagnetic dopant conditions at 80 K, which determine the value of T_{1n}), but are still much greater than 100 at the lower temperatures. These low-temperature results compare favorably with DNP enhancements obtained at higher temperatures with higher microwave powers [3,17,18,46].

3.2 Effect of field modulation during DNP

Figure 6 shows the effect of magnetic field modulation during DNP on the observed signal enhancements for various dopant conditions and temperatures. In all cases, field modulation at 2–6 kHz with a root-mean-squared (rms) amplitude of 10–40 G (28–112 MHz rms modulation of the EPR frequency) produces significant increases in ξ_T. Field modulation effects are also summarized in Table 1. The results from various samples indicate that the effect is generally stronger at lower doping concentrations, and slightly stronger at higher temperatures. As seen in Figure 6b, the dependence on modulation frequency does not vary strongly with microwave power level, modulation amplitude, or temperature. The only factor that produces clear differences in the frequency dependence is the identity of the nitroxide dopant, as seen in Figure 6d. For the dopant concentrations measured, the required modulation frequency increases as the number of nitroxide moieties in the dopant increases. T_{DNP} has the

same value with and without field modulation, to within experimental error (see Figure S2 of Supplementary Material). Thus, the initial rate of increase of the ^{1}H spin polarization is greater with field modulation, but the time constant for approaching the maximum achievable polarization is the same. As explained below, we attribute this observation to an increased fractional saturation of the total electron spin system in the presence of field modulation.

3.3 Temperature and power dependence of DNP enhancements

Figure 7 shows the full temperature dependencies of T_{DNP} and the DNP sensitivity enhancement over the 7–80 K range for a single sample with 30 mM DOTOPA-TEMPO and without field modulation. Relative to ^{1}H NMR measurements on the same sample without microwave radiation at 80 K, sensitivity enhancement factors greater than 50 are obtained at temperatures at 35 K and below. Factors greater than 100 are obtained at temperatures at 20 K and below. This temperature range is relevant to low-temperature biomolecular solid state NMR experiments under magic-angle spinning (MAS) when liquid helium is used to cool the sample [47].

Finally, we observe nearly linear dependencies of DNP signal enhancements on microwave power at 35 K for samples doped with 4-amino-TEMPO, TOTAPOL, and DOTOPA-TEMPO, suggesting that a higher-power microwave source would be beneficial (see Figure S3 of Supplementary Material). With 30 mM DOTOPA-TEMPO at 7 K, the signal enhancement appears to saturate above 20 mW. This behavior may be due to sample heating at the higher microwave powers, which is likely to be more pronounced at the low-temperature limit of our cryostat. Higher microwave powers would then be beneficial if the thermal contact between the sample and the temperature-controlled copper block in our cryostat could be improved.

4. Discussion

4.1 Mechanism for enhancement of DNP by field modulation

Figure 6 and Table 1 show that field modulation during microwave irradiation increases DNP enhancements of ^{1}H NMR signals by factors of 1.1–2.4 under our experimental conditions, depending on temperature, dopant, and dopant concentration. The basis for this effect is that electron spin diffusion is not rapid enough to spread the microwave-induced reduction of electron spin polarization (*i.e.*, electron spin saturation) across the inhomogeneously broadened EPR line on a time scale that is limited by the electron spin-lattice relaxation time T_{1e}. The microwaves therefore saturate a small fraction of the electron spins, in a narrow frequency range within the EPR lineshape. Field (or frequency) modulation can increase this frequency range, thereby increasing the number of electron spins that participate in DNP.

To quantify the effect of field modulation on electron spin saturation, we performed simulations of the evolution of electron spin polarization within an inhomogeneously broadened EPR line (represented by 500 electron spin "packets", spaced equally over a 430 MHz frequency range) in the presence of a fixed-frequency, circularly-polarized microwave field with amplitude B_1, sinusoidal field modulation of the main field B_0, and longitudinal and transverse spin relaxation rates $1/T_{1e}$ and $1/T_{2e}$. Starting with longitudinal polarization of unity in each packet (representing thermal equilibrium), the time dependence of the polarization for each packet was determined by numerical solution of the Bloch equations, using time steps of 0.2 μs during which the value of B_0 was considered to be constant. In each time step, the rotation of the spin polarization produced by the microwave field and the frequency offset was calculated analytically and applied to each spin packet. The longitudinal polarization of each spin packet was then relaxed towards equilibrium and the transverse polarization was relaxed towards zero by amounts appropriate for one time step with the assumed values of T_{1e} and T_{2e}. In addition to this independent evolution of each spin packet, spectral diffusion of electron spin

polarization was included by allowing partial exchange of longitudinal polarization between packets with adjacent EPR frequencies after each time step. The spectral diffusion constant D is defined by the relation $D = k_{ex}\Delta^2$, where Δ is frequency spacing between the spin packets that exchange polarization at rate k_{ex}. The electron spin system was allowed to reach a quasi-steady state in the presence of B1 and the modulated B_0 by evolving for a time period $4T_{1e}$. The simulation was then continued for one additional field modulation cycle, during which the time-averaged longitudinal polarization $S_{z,ave}$ of each spin packet was calculated. The average saturation value for each packet is given by $1 - S_{z,ave}$.

For simplicity, we use a uniform spacing of electron spin packets across the frequency region of interest. This also means that the electron dipolar reservoir can be safely neglected. Because the simulation is symmetric, spectral diffusion produces no net change in Zeeman energy. Zeeman energy flow from momentary asymmetries due to the direction of the modulation is not sufficient to perturb the electron dipolar system from thermal equilibrium significantly.

DNP enhancements of ^{1}H NMR signals through a cross-effect mechanism at 9.4 T are expected to be proportional to the total sum of electron spin polarization differences for spin pairs whose EPR frequencies differ by 400 MHz [21]. As verified by the simulations discussed below, electron spins that are off-resonance by 400 MHz are not perturbed significantly by microwave irradiation, so that the relevant spin polarization differences are simply proportional to the saturation of the electron spin polarizations near resonance. Thus, we can assume that DNP enhancements are nearly proportional to the total electron spin saturations in our simulations.

All parameters required for these simulations can be estimated from experiments. Our simulations use parameters appropriate for 40 mM 4-amino-TEMPO, because of the availability of the data of Farrar *et al*. for 40 mM 4-amino-TEMPO at 5.0 T and 11 K [21]. For the direct spin-lattice relaxation process at high temperature, $1/T_{1e} \propto B_0{}^4T$ [48–50]. From the value T_{1e} = 75 ms reported by Farrar *et al*., we therefore estimate that T_{1e} = 2 ms at 9.4 T and 35 K. For an EPR line dominated by g-anisotropy, electron spin diffusion is expected to weaken at higher field because the electron concentration in frequency space decreases linearly with increasing field. Farrar *et al*. fit their data for 40 mM 4-amino-TEMPO with $k_{ex} = 2.5 \times 10^7$ s^{-1} and $\Delta = 1.8 \times 10^6$ s^{-1}, resulting in $D \approx 8 \times 10^{17}$ Hz^2/s. Assuming that the electron spin diffusion rate is proportional to the square of the frequency-space concentration (*i.e*., that k_{ex} for a given value of Δ is inversely proportional to $B_0{}^2$), we estimate that $D \approx 2 \times 10^{17}$ Hz^2/s for 40 mM 4-amino-TEMPO at 9.4 T. For T_{2e}, we use the value of 4 μs from low field measurements [48]. Our simulations are insensitive to variations of T_{2e} by a factor of two above or below this value. Assuming that the microwave beam passing through our RF coil (3.2 mm inner diameter) carries 15 mW of power, we calculate the microwave B_1 field to be 0.03 G (corresponding to an 80 kHz Rabi frequency for electron spins).

Figure 8 shows the calculated dependence of the frequency profile of electron spin saturation, averaged over one modulation period as described above, on field modulation amplitude with 10 kHz modulation. Although the saturation value for electron spins in the center of the profile decreases when the modulation amplitude increases, the total saturation increases. Assuming that the DNP enhancement of ^{1}H NMR signals is proportional to the total electron spin saturation, this accounts for the increased DNP enhancement under field modulation. As shown in Figure 6d, the simulated frequency dependence of the DNP enhancement is in reasonable agreement with the experimental frequency dependence, with both showing increased DNP as the modulation frequency becomes comparable to $1/T_{1e}$. The simulation shows a tripling (200% increase) of the DNP signal with rapid field modulation, compared to the experimental increase of 135% for 4-amino-TEMPO at 35 K. At modulation frequencies above 2 kHz, both the calculated total electron spin saturation and the experimental DNP enhancement become independent of modulation frequency. This behavior reflects the fact that, once the modulation

frequency greatly exceeds $1/T_{1e}$, the average saturation of a given spin packet depends only on the fraction of time that the spin packet is nearly on-resonance with the microwaves.

The dependence of the simulated electron spin saturation on the various parameters is shown in Figure 9. Larger values of the modulation amplitude, the spectral diffusion constant, T_{1e}, and B_1 all increase the total saturation. Minor variations in the frequency dependence are observed as these parameters change. The comparison between the simulations and 4-amino-TEMPO data in Figure 6d suggests that some combination of a longer T_{1e}, a weaker B_1, and perhaps a different spectral diffusion rate than estimated above would produce better agreement. For TOTAPOL and DOTOPA-TEMPO, the effect of field modulation is weaker, and faster modulation is required for the maximum effect. This is primarily consistent with faster spectral diffusion, which causes both of those effects in the simulations in Figure 9b. Faster spectral diffusion in TOTAPOL and DOTOPA-TEMPO solutions is certainly plausible, as these solutions contain groups of two or three strongly coupled spins, which may accelerate spectral diffusion.

Overall, the agreement between simulations and the experimental data is satisfactory, considering uncertainties in the estimation of the relevant parameters from lower-field experiments. The simulations indicate that the dependence on modulation frequency primarily reflects the T_{1e} value, while the size of the effect on DNP enhancements depends on B_1, T_{1e}, spectral diffusion, and the modulation amplitude (but not on T_{2e}).

The benefit of field and/or frequency modulation in DNP experiments has been observed previously at lower fields and lower temperatures. However, the mechanisms used to explain the effect do not seem to apply in our case: (1) A frequency modulation enhancement was seen at 2.5 T and 0.3 K in the context of DNP for polarized particle physics targets [51,52]. The explanation by Kisselev [51] relies on changes of microwave propagation in the sample due to interaction of the microwaves with the electron spin resonance. However, primarily because our sample is only 3 mm thick, rather than 50 cm as in Kisselev's experiments, we expect this effect to be negligible in our experiments; (2) In studies of microwave-induced optical nuclear spin polarization in molecular crystals by Schmidt, Wenkebach, and coworkers, the effect of both field and frequency modulation was studied at 0.3 T and 2.7 T over the 1.2–1.4 K temperature range [53–55]. By applying simultaneous in-phase field and frequency modulation, Wenckebach *et al*. showed that different mechanisms were operating at the two magnetic fields [55]. In the first mechanism (at low fields), field or frequency modulation enhances total nuclear spin polarizations by overcoming a limit imposed by slow nuclear spin diffusion. In our experiments, the relatively high concentrations of nitroxide dopants suggests that nuclear spin diffusion is not a limiting factor. In the second mechanism (at higher fields), DNP is limited by the poor efficiency of electron spin-lattice relaxation through phonon scattering (sometimes called a phonon bottleneck). Since our experiments are performed on glycerol/water glasses, rather than single crystals, we expect the phonon lifetime to be on the order of 100 ps [56], rather than the 0.14 μs estimated from the single-crystal experiments [54]. The shorter phonon lifetime makes it unlikely that a phonon bottleneck limits DNP enhancements in our experiments.

4.2 Additional implications and future prospects

It is informative to consider the microwave power absorbed by electron spins under experimental conditions similar to ours. Given a sample volume of 10 μl, an electron spin concentration of 40 mM, $T_{1e} \approx 2$ ms, and $B_0 = 9.4$ T, the power required to maintain the electron spins in a fully saturated state would be approximately 20 mW. According to the simulations described above, we are saturating less than 10% of the spins, up to roughly 70% saturation, implying approximately 1 mW power consumption. In principle, the DNP enhancements of ^{1}H NMR signals could be increased by placing the sample in a cavity or resonator that boosts

the B_1 field within the sample. Since the power consumed in saturating the electron spins represents about 3% of the input microwave power in our experiments, such a cavity could not have a quality factor (Q) greater than 30. Nonetheless, even a cavity with $Q < 10$ might result in significant improvements.

Building on the earlier demonstrations by Griffin and coworkers that biradical dopants are advantageous for high-field DNP [17,18], data presented above show that a triradical dopant can provide larger DNP enhancements and more rapid DNP build-up rates under our experimental conditions. Dopants containing four or more nitroxide moieties [39,57] may provide further improvements, although we have not yet tested this possibility.

We attribute the DNP enhancements in our experiments to the cross effect, rather than thermal mixing, because the inhomogeneous EPR linewidth, due to g-anisotropy, is approximately twice the ^{1}H NMR frequency (see Figure 4), while the homogeneous EPR linewidth is roughly one order of magnitude less than the ^{1}H NMR frequency. The DNP buildup rate under the cross effect should be proportional to the square of the electron-electron dipolediple coupling, partially explaining the greater build-up rates observed with biradical and triradical dopants.

The VDI microwave source used in our experiments provides only 30 mW at 264 GHz, but is compact, relatively inexpensive, and (in our experience to date) reliable. The quasi-optical system converts the linearly polarized output of the microwave source to a circularly polarized state, so that all of the available microwave power can be used to saturate electron spin polarizations. Although the resulting DNP enhancements are relatively small at 80 K, they are large at lower temperatures (see Figure 7 and Table 1). Thus, we expect this apparatus to provide NMR sensitivity enhancements that are sufficient to enable a variety of experiments on biomolecular systems that would otherwise be impractical. As one important example, we plan to combine this microwave system with a low-temperature MAS probe that we have recently developed for biomolecular studies at 25 K [47]. In the context of MAS experiments, it is worth noting that sample rotation at speeds greater than 2 kHz produces a natural modulation of EPR frequencies, through g-anisotropy, that resembles (but exceeds) the EPR frequency variations produced by field modulation in the experiments described above. DNP enhancements under MAS may be larger than those observed in our experiments on non-spinning samples. It may prove useful to combine field or frequency modulation with MAS, or to gate the microwave field in synchrony with MAS, in order to optimize the DNP enhancements.

In addition to MAS experiments, structural studies of aligned samples, such as integral membrane proteins and peptides in aligned phospholipid bilayers [58], should be feasible with the microwave apparatus and cryostat described above. This apparatus may also be useful in magnetic resonance micro-imaging experiments [59,60], where sensitivity enhancements obtained through low-temperature DNP may permit imaging at sub-micron scales.

Supplementary Material

Refer to Web version on PubMed Central for supplementary material.

Acknowledgments

We thank Bernie Howder for machining parts for our cryostat and Dr. Murali C. Krishna for use of the X-band EPR spectrometer. We thank Dr. Kan-Nian Hu for many useful discussions regarding DNP effects and experimental methods. This work was supported by the Intramural Research Program of the National Institute of Diabetes and Digestive and Kidney Diseases of the National Institutes of Health, and by the NIH Intramural AIDS Targeted Antiviral Program. This study utilized the high-performance computational capabilities of the Biowulf Linux cluster at the NIH (http://biowulf.nih.gov).

References

1. Overhauser AW. Polarization of nuclei in metals. Phys. Rev 1953;92:411–415.
2. Carver TR, Slichter CP. Polarization of nuclear spins in metals. Phys. Rev 1953;92:212–213.
3. Maly T, Debelouchina GT, Bajaj VS, Hu KN, Joo CG, Mak-Jurkauskas ML, Sirigiri JR, van der Wel PCA, Herzfeld J, Temkin RJ, Griffin RG. Dynamic nuclear polarization at high magnetic fields. J. Chem. Phys 2008;128:052211. [PubMed: 18266416]
4. Prisner T, Kockenberger W. Dynamic nuclear polarization: New experimental and methodology approaches and applications in physics chemistrybiology and medicine. Appl. Magn. Reson 2008;34:213–218.
5. Wind RA, Duijvestijn MJ, Vanderlugt C, Manenschijn A, Vriend J. Applications of dynamic nuclear polarization in ^{13}C NMR in solids. Prog. Nucl. Magn. Reson. Spectrosc 1985;17:33–67.
6. Singel DJ, Seidel H, Kendrick RD, Yannoni CS. A spectrometer for EPR, DNP, and multinuclear high-resolution NMR. J. Magn. Reson 1989;81:145–161.
7. Afeworki M, McKay RA, Schaefer J. Selective observation of the interface of heterogeneous polycarbonate polystyrene blends by dynamic nuclear polarization ^{13}C NMR spectroscopy. Macromolecules 1992;25:4084–4091.
8. Becerra LR, Gerfen GJ, Temkin RJ, Singel DJ, Griffin RG. Dynamic nuclear polarization with a cyclotron resonance maser at 5 T. Phys. Rev. Lett 1993;71:3561–3564. [PubMed: 10055008]
9. Bajaj VS, Farrar CT, Hornstein MK, Mastovsky I, Vieregg J, Bryant J, Elena B, Kreischer KE, Temkin RJ, Griffin RG. Dynamic nuclear polarization at 9 T using a novel 250 GHz gyrotron microwave source. J. Magn. Reson 2003;160:85–90. [PubMed: 12615147]
10. Bajaj VS, Hornstein MK, Kreischer KE, Sirigiri JR, Woskov PP, Mak-Jurkauskas ML, Herzfeld J, Temkin RJ, Griffin RG. 250 GHz cw gyrotron oscillator for dynamic nuclear polarization in biological solid state NMR. J. Magn. Reson 2007;189:251–279. [PubMed: 17942352]
11. Idehara T, Saito T, Ogawa I, Mitsudo S, Tatematsu Y, Agusu L, Mori H, Kobayashi S. Development of terahertz FUCW gyrotron series for DNP. Appl. Magn. Reson 2008;34:265–275.
12. Becerra LR, Gerfen GJ, Bellew BF, Bryant JA, Hall DA, Inati SJ, Weber RT, Un S, Prisner TF, McDermott AE, Fishbein KW, Kreischer KE, Temkin RJ, Singel DJ, Griffin RG. A spectrometer for dynamic nuclear polarization and electron paramagnetic resonance at high frequencies. J. Magn. Res. A 1995;117:28–40.
13. Weis V, Bennati M, Rosay M, Bryant JA, Griffin RG. High-field DNP and ENDOR with a novel multiple-frequency resonance structure. J. Magn. Reson 1999;140:293–299. [PubMed: 10479576]
14. Weis V, Bennati M, Rosay M, Griffin RG. Solid effect in the electron spin dressed state: A new approach for dynamic nuclear polarization. J. Chem. Phys 2000;113:6795–6802.
15. Farrar CT, Hall DA, Gerfen GJ, Rosay M, Ardenkjaer-Larsen JH, Griffin RG. High-frequency dynamic nuclear polarization in the nuclear rotating frame. J. Magn. Reson 2000;144:134–141. [PubMed: 10783283]
16. Rosay M, Zeri AC, Astrof NS, Opella SJ, Herzfeld J, Griffin RG. Sensitivityenhanced NMR of biological solids: Dynamic nuclear polarization of Y21M fd bacteriophage and purple membrane. J. Am. Chem. Soc 2001;123:1010–1011. [PubMed: 11456650]
17. Song CS, Hu KN, Joo CG, Swager TM, Griffin RG. TOTAPOL: A biradical polarizing agent for dynamic nuclear polarization experiments in aqueous media. J. Am. Chem. Soc 2006;128:11385–11390. [PubMed: 16939261]
18. Hu KN, Song C, Yu HH, Swager TM, Griffin RG. High-frequency dynamic nuclear polarization using biradicals: A multifrequency EPR lineshape analysis. J. Chem. Phys 2008;128:052302. [PubMed: 18266419]
19. Matsuki Y, Maly T, Ouari O, Karoui H, Le Moigne F, Rizzato E, Lyubenova S, Herzfeld J, Prisner T, Tordo P, Griffin RG. Dynamic nuclear polarization with a rigid biradical. Angew. Chem. Int. Edit 2009;48:4996–5000.
20. Kessenikh AV, Lushchikov VI, Manenkov AA, Taran YV. Proton polarization in irradiated polyethylenes. Sov. Phys.-Sol. State 1963;5:321–329.
21. Farrar CT, Hall DA, Gerfen GJ, Inati SJ, Griffin RG. Mechanism of dynamic nuclear polarization in high magnetic fields. J. Chem. Phys 2001;114:4922–4933.

22. Granwehr J, Kockenberger W. Multidimensional low-power pulsed EPR under DNP conditions. Appl. Magn. Reson 2008;34:355–378.
23. Jenista ER, Branca RT, Warren WS. Hyperpolarized carbon-carbon intermolecular multiple quantum coherences. J. Magn. Reson 2009;196:74–77. [PubMed: 18926750]
24. Johanneson H, Macholl S, Ardenkjaer-Larsen JH. Dynamic nuclear polarization of [1-^{13}C]pyruvic acid at 4.6 Tesla. J. Magn. Reson 2009;197:167–175. [PubMed: 19162518]
25. Kurdzesau F, van den Brandt B, Comment A, Hautle P, Jannin S, van der Klink JJ, Konter JA. Dynamic nuclear polarization of small labelled molecules in frozen wateralcohol solutions. J. Phys. D 2008;41
26. Zeng H, Bowen S, Hilty C. Sequentially acquired two-dimensional NMR spectra from hyperpolarized samples. J. Magn. Reson 2009;199:159–165. [PubMed: 19447055]
27. Prandolini MJ, Denysenkov VP, Gafurov M, Endeward B, Prisner TF. High-field dynamic nuclear polarization in aqueous solutions. J. Am. Chem. Soc 2009;131:6090–6092. [PubMed: 19361195]
28. Giraudeau P, Shrot Y, Frydman L. multiple ultrafast, broadband 2D NMR spectra of hyperpolarized natural products. J. Am. Chem. Soc 2009;131:13902–13903. [PubMed: 19743849]
29. Cho H, Baugh J, Ryan CA, Cory DG, Ramanathan C. Low temperature probe for dynamic nuclear polarization and multiple-pulse solid state NMR. J. Magn. Reson 2007;187:242–250. [PubMed: 17524687]
30. Morley GW, van Tol J, Ardavan A, Porfyrakis K, Zhang JY, Briggs GAD. Efficient dynamic nuclear polarization at high magnetic fields. Phys. Rev. Lett 2007;98
31. Weliky DP, Bennett AE, Zvi A, Anglister J, Steinbach PJ, Tycko R. Solid state NMR evidence for an antibody-dependent conformation of the V3 loop of HIV-1 gp120. Nature Struct. Biol 1999;6:141–145. [PubMed: 10048925]
32. Blanco FJ, Hess S, Pannell LK, Rizzo NW, Tycko R. Solid state NMR data support a helix-loop-helix structural model for the N-terminal half of HIV-1 Rev in fibrillar form. J. Mol. Biol 2001;313:845–859. [PubMed: 11697908]
33. Sharpe S, Kessler N, Anglister JA, Yau WM, Tycko R. Solid state NMR yields structural constraints on the V3 loop from HIV-1 gp120 bound to the 447-52d antibody Fv fragment. J. Am. Chem. Soc 2004;126:4979–4990. [PubMed: 15080704]
34. Havlin RH, Tycko R. Probing site-specific conformational distributions in protein folding with solid state NMR. Proc. Natl. Acad. Sci. U.S.A 2005;102:3284. [PubMed: 15718283]
35. Havlin RH, Blanco FJ, Tycko R. Constraints on protein structure in HIV-1 Rev and Rev-RNA supramolecular assemblies from two-dimensional solid state nuclear magnetic resonance. Biochemistry 2007;46:3586–3593. [PubMed: 17311419]
36. Hu KN, Havlin RH, Yau WM, Tycko R. Quantitative determination of site-specific conformational distributions in an unfolded protein by solid state nuclear magnetic resonance. J. Mol. Biol 2009;392:1055–1073. [PubMed: 19647001]
37. Hu K-N, Yau W-M, Tycko R. Detection of a transient intermediate in a rapid protein folding process by solid state nuclear magnetic resonance. J. Am. Chem. Soc 2010;132:24–25. [PubMed: 20000466]
38. Atherton, NM. Principles of Electron Spin Resonance. New York: Ellis Horwood, Ltd; 1993.
39. Turro NJ, Khudyakov IV, Bossmann SH, Dwyer DW. An electron spin polarization study of the interaction of photoexcited triplet molecules with mononitroxyl and polynitroxyl stable free radicals. J. Phys. Chem 1993;97:1138–1146.
40. Luckhurst GR. Alternating linewidths. A novel relaxation process in the electron resonance of biradicals. Mol. Phys 1966;10:543.
41. Paleos CM, Dais P. Ready reduction of some nitroxide free radicals with ascorbic acid. J. Chem. Soc.-Chem. Commun 1977:345–346.
42. Wylde RJ. Millimetre wave Gaussian beam mode optics and corrugated feed horns. IEEE Proc 1984;131H:258–262.
43. Lesurf, JCG. Millimetre-Wave Optics. New York: Devices & Systems, Taylor & Francis; 1990.
44. Doane, JL. Propagation and mode coupling in corrugated and smooth-wall circular waveguies. In: Button, KJ., editor. Infrared and Millimeter Waves. Vol. Vol. 13. New York: Academic Press, Inc; 1985. p. 123-170.

45. Wollan DS. Dynamic nuclear polarization with an inhomogeneously broadened ESR line. 1. Theory. Phys. Rev. B 1976;13:3671–3685.
46. Hu KN, Bajaj VS, Rosay M, Griffin RG. High-frequency dynamic nuclear polarization using mixtures of TEMPO and trityl radicals. J. Chem. Phys 2007;126:044512. [PubMed: 17286492]
47. Thurber KR, Tycko R. Biomolecular solid state NMR with magic angle spinning at 25 K. J. Magn. Reson 2008;195:179–186. [PubMed: 18922715]
48. Sato H, Kathirvelu V, Spagnol G, Rajca S, Rajca A, Eaton SS, Eaton GR. Impact of electron-electron spin interaction on electron spin relaxation of nitroxide diradicals and tetraradicals in glassy solvents between 10 and 300 K. J. Phys. Chem. B 2008;112:2818–2828. [PubMed: 18284225]
49. Kronig RD. On the mechanism of paramagnetic relaxation. Physica 1939;6:33–43.
50. Scott PL, Jeffries CD. Spin-lattice relaxation in some rare-earth salts at helium temperatures: Observation of a phonon bottleneck. Phys. Rev 1962;127:32–51.
51. Kisselev YF. The polarized target technique. Phys. Part. Nuclei 2000;31:354–380.
52. Kisselev YF. The modulation effect on the dynamic polarization of nuclear spins. Nucl. Instrum. Meth. A 1995;356:99–101.
53. Vankesteren HW, Wenckebach WT, Schmidt J. The mechanism of microwave-induced optical nuclear polarization in fluorene doped with phenanthrene: A qualitative analysis. Chem. Phys. Lett 1985;121:440–445.
54. Verheij PFA, Wenckebach WT, Schmidt J. Microwave-induced optical nuclearpolarization at 75 GHz: A quantitative analysis. Appl. Magn. Reson 1993;5:187–205.
55. Wenckebach WT. Thermodynamics of dynamic nuclear polarization. Nucl. Instrum. Meth. A 1995;356:1–4.
56. Ruocco G, Sette F, Di Leonardo R, Fioretto D, Krisch M, Lorenzen M, Masciovecchio C, Monaco G, Pignon F, Scopigno T. Nondynamic origin of the high frequency attenuation in glasses. Phys. Rev. Lett 1999;83:5583–5586.
57. Maliakal AJ, Turro NJ, Bosman AW, Cornel J, Meijer EW. Relaxivity studies on dinitroxide and polynitroxyl functionalized dendrimers: Effect of electron exchange and structure on paramagnetic relaxation enhancement. J. Phys. Chem. A 2003;107:8467–8475.
58. De Angelis, AA.; Jones, DH.; Grant, CV.; Park, SH.; Mesleh, MF.; Opella, SJ. NMR experiments on aligned samples of membrane proteins. In: James, T., editor. Nuclear Magnetic Resonance of Biological Macromolecules, Part C, Methods in Enzymology. Vol. Vol. 394. San Diego: Academic Press; 2005. p. 350-382.
59. Ciobanu L, Pennington CH. 3D micron-scale MRI of single biological cells. Solid State Nucl. Magn. Reson 2004;25:138–141. [PubMed: 14698400]
60. Seeber DA, Cooper RL, Ciobanu L, Pennington CH. Design and testing of a high sensitivity microreceiver coil apparatus for nuclear magnetic resonance and imaging. Rev. Sci. Instrum 2001;72:2171–2179.

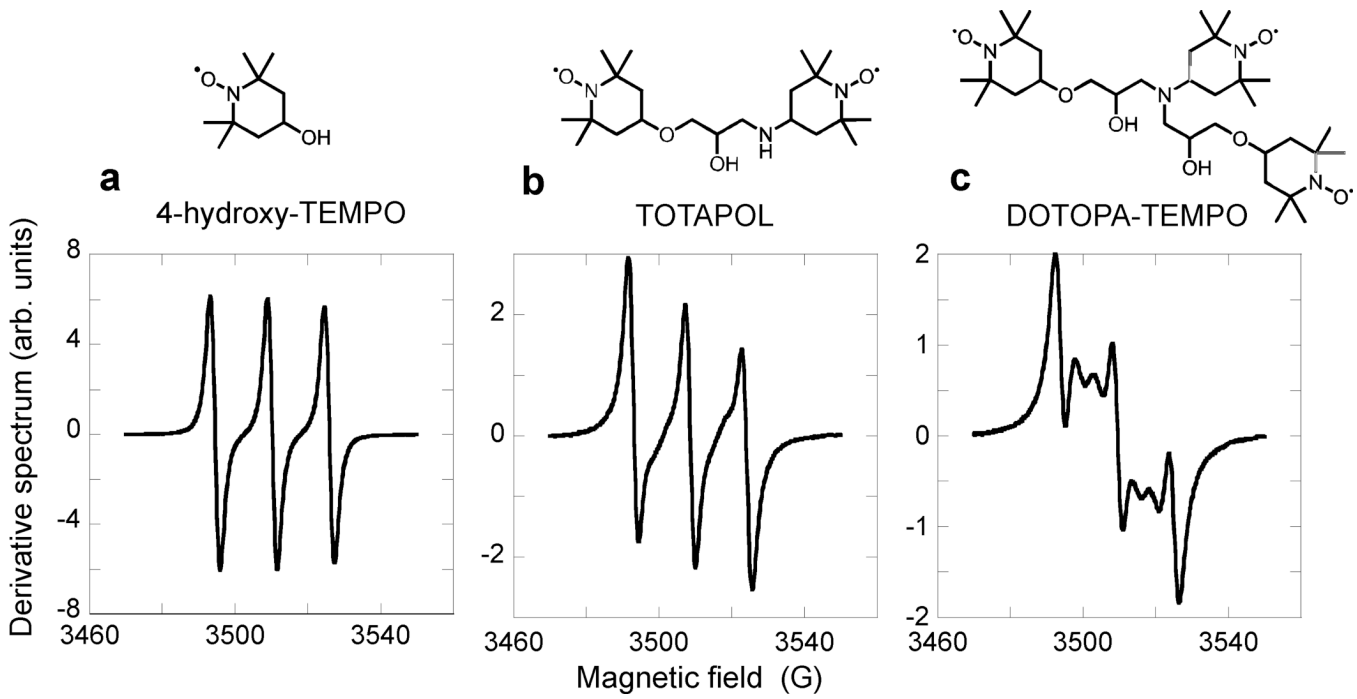

Figure 1.
X-band EPR spectra and chemical structures of 4-hydroxy-TEMPO (a), TOTAPOL (b), and DOTOPA-TEMPO (c). All samples are 0.5 mM solutions in 95/5 vol% ethanol/water at room temperature.

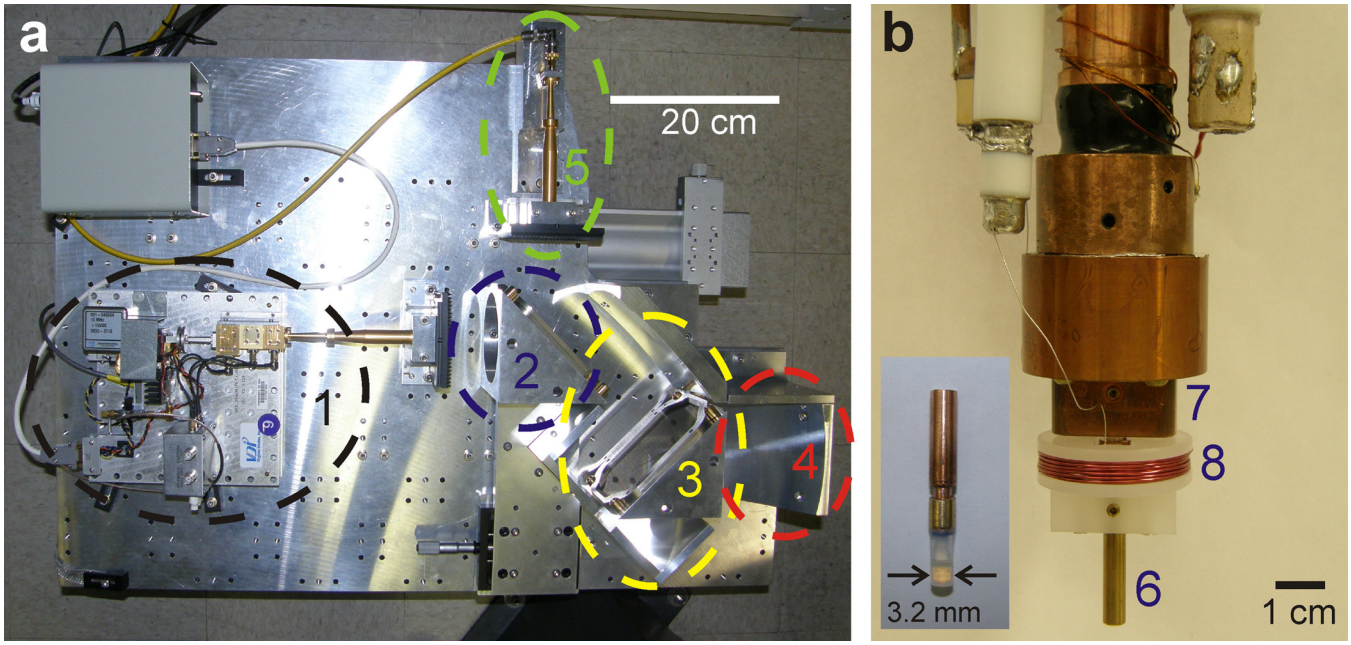

Figure 2.

(a) Photograph of the quasi-optical microwave system, including the 264 GHz microwave source with corrugated horn (1), wire grid polarizer (2), Martin-Puplett interferometer for polarization control (3), mirror (4), and corrugated horn with detector for EPR measurements (5). In DNP and EPR experiments the entire plate is positioned at the base of a 9.39 T wide-bore superconducting NMR magnet, with the mirror directly below the vertical magnet bore. The mirror directs the microwave beam into a corrugated waveguide in the bore, which transmits the beam to the bottom of the cryostat. (b) Photograph of the head of the cryostat, with the outer vacuum can and radiation shield removed. Microwaves pass through a polyethylene window in the bottom of the vacuum can and enter the brass tube (6). The sample is attached to and cooled by the temperature-controlled copper block (7). The sample and RF coil are at the center of the field modulation coil (8). The inset shows the glycerol/water sample, which is contained within a translucent Teflon cup that makes a vacuum-tight seal with a copper rod, which in turn attaches to the temperature-controlled block. Thermal contact to the copper is provided by a sapphire rod within the Teflon cup.

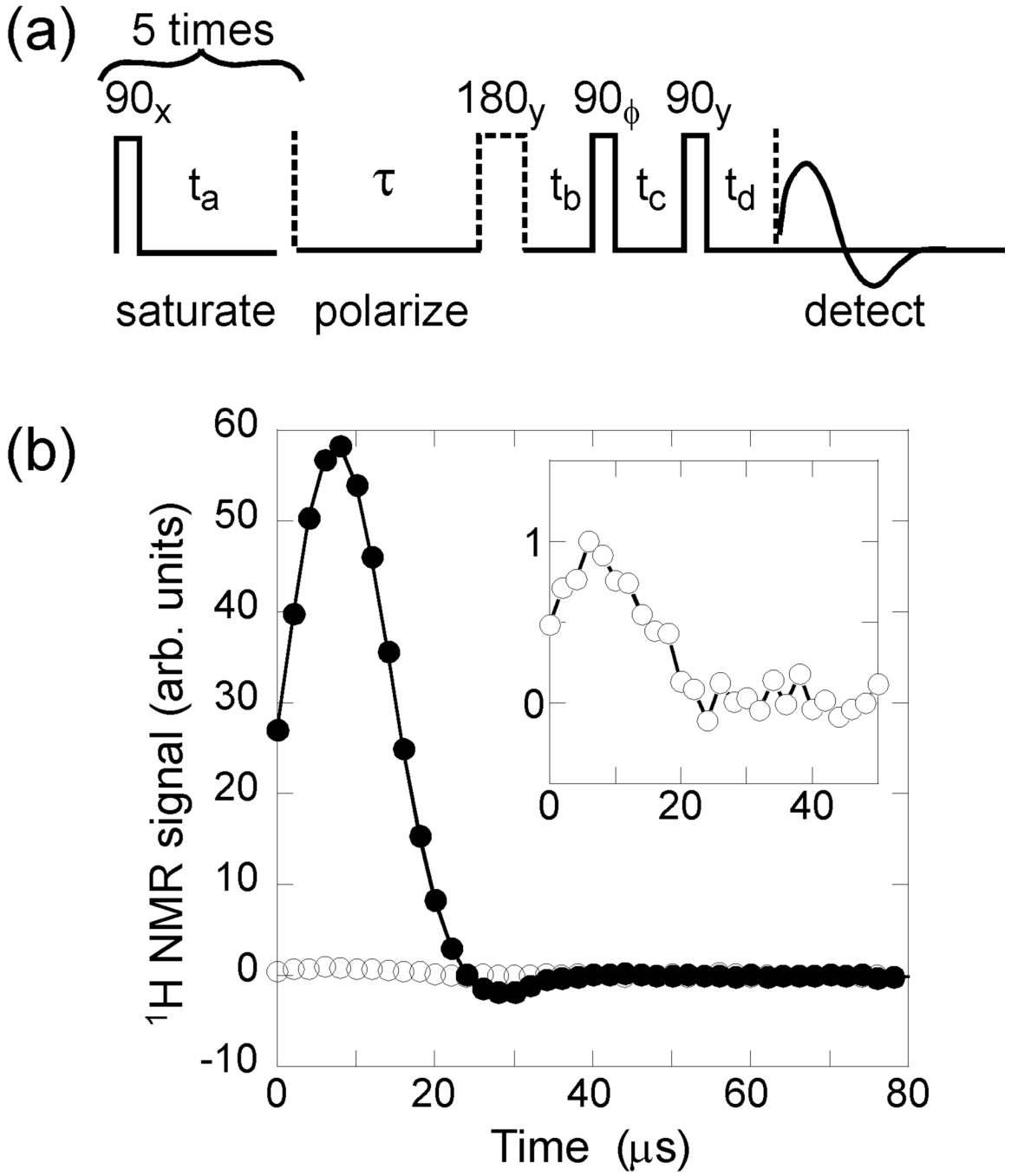

Figure 3.

(a) Radio-frequency pulse sequence for ^{1}H NMR and DNP measurements. 90° pulse lengths were 6–8 μs, t_a = 200 μs, t_b = 100 μs, t_c = 20 μs, and t_d = 14 μs. The 180° pulse was applied on alternating scans, ϕ followed the pattern x, x, −x, −x, and successive echo signals were co-added with the sign pattern +, −, −, +. (b) ^{1}H NMR solid echo signals with DNP-enhanced ^{1}H spin polarization (●) and with thermal equilibrium polarization (○) at 11 K. The inset shows the thermal equilibrium signal on an expanded scale. The sample is 30 mM DOTOPA-TEMPO in 10 μl of 25/75 mol% glycerol/water, pH 3 (0.22 M acetate buffer). The microwave frequency

and power are 264.0 GHz and 30 mW. Each echo signal is the result of four scans with $\tau = 12$ s.

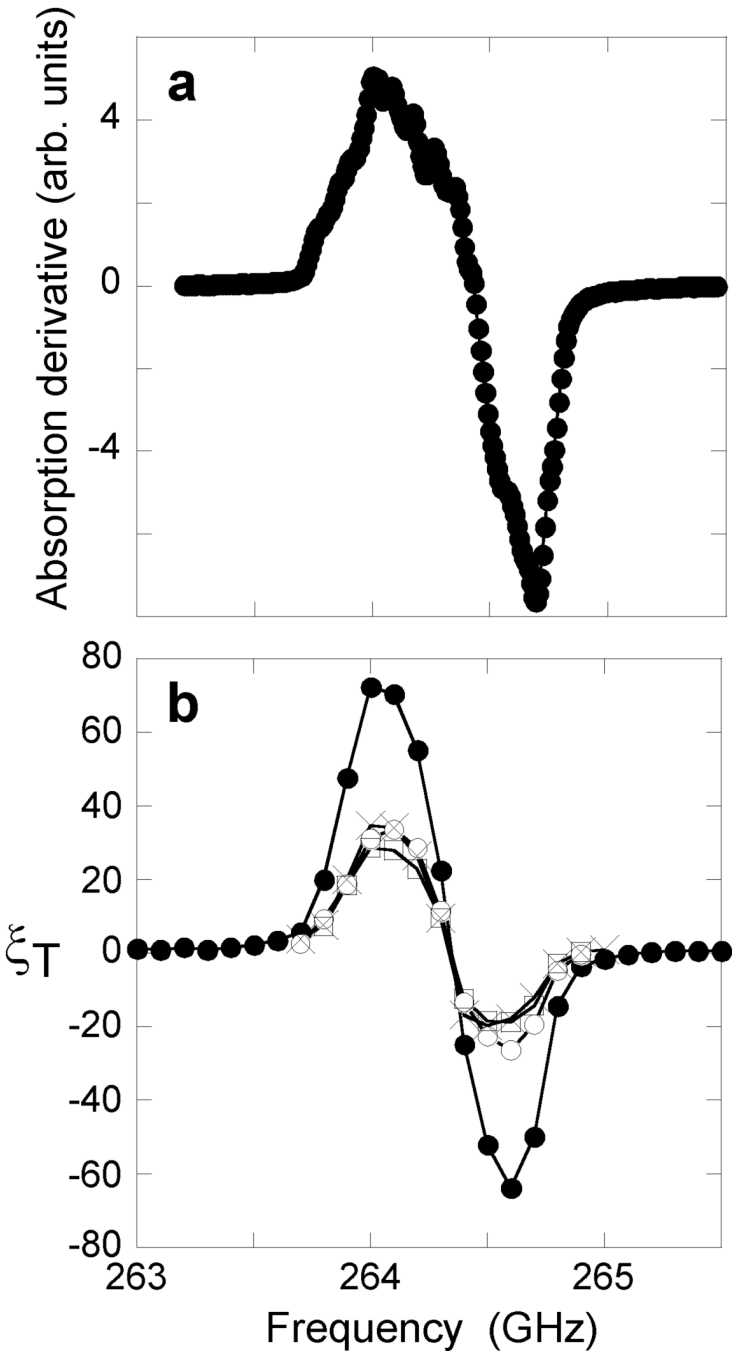

Figure 4.

(a) EPR absorption derivative spectrum of 40 mM 4-amino-TEMPO in glycerol/water at 16 K, recorded at 9.4 T in the DNP cryostat. Small oscillations in the absorption derivative are primarily artifacts from microwave power variations caused by interference effects within the quasi-optical system. (b) DNP signal enhancements as a function of microwave frequency for 20 mM DOTOPA-TEMPO at 16 K (●), 20 mM DOTOPA-TEMPO at 35 K (○),20 mM TOTAPOL at 16 K (□), and 40 mM 4-amino-TEMPO at 16 K (×). All samples are 10 μl of 25/75 mol% glycerol/water. Lines are drawn to guide the eye.

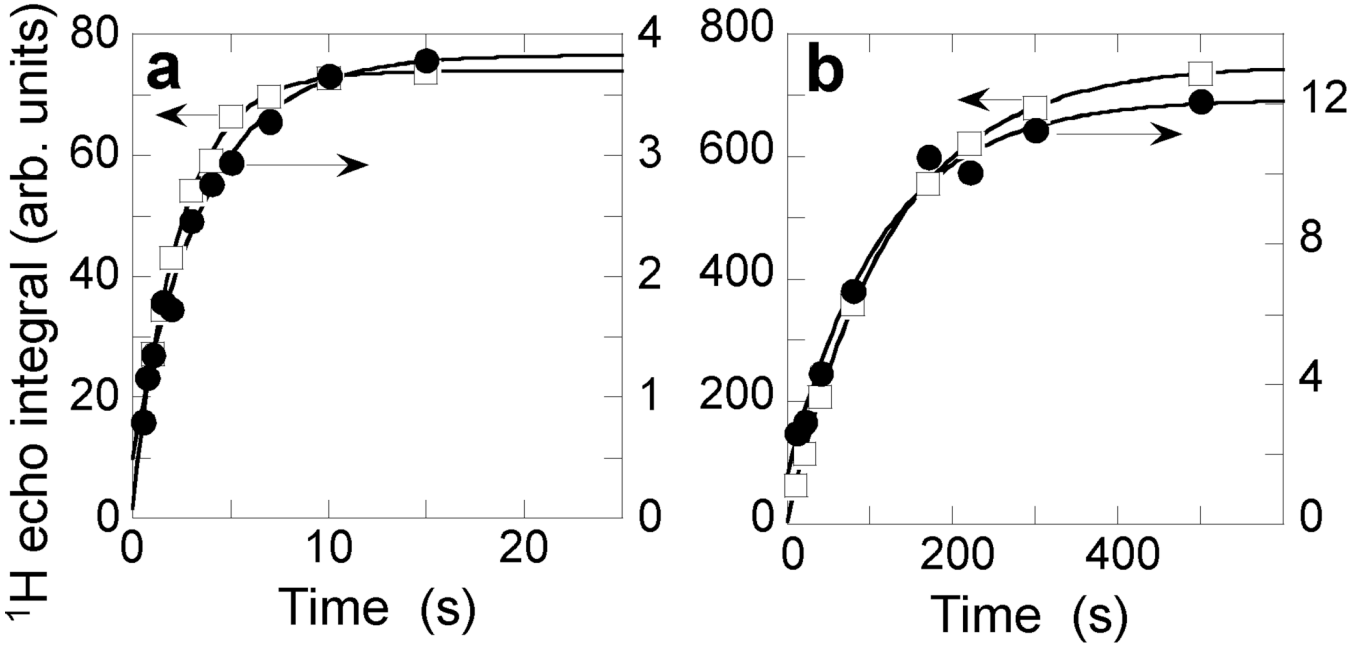

Figure 5.

Build-up of ^{1}H spin polarization after saturation with DNP (□) and without DNP (●) for 160 mM 4-amino-TEMPO at 35 K (a) and 40 mM 4-amino-TEMPO at 16 K (b). Lines are fits to exponential recovery curves, with an offset from zero to account for background signal or imperfect saturation. Time constants are 2.4 ± 0.2 s with DNP and 3.5 ± 0.8 s without DNP in panel a, and 126 ± 6 s with DNP and 115 ± 30 s without DNP in panel b.

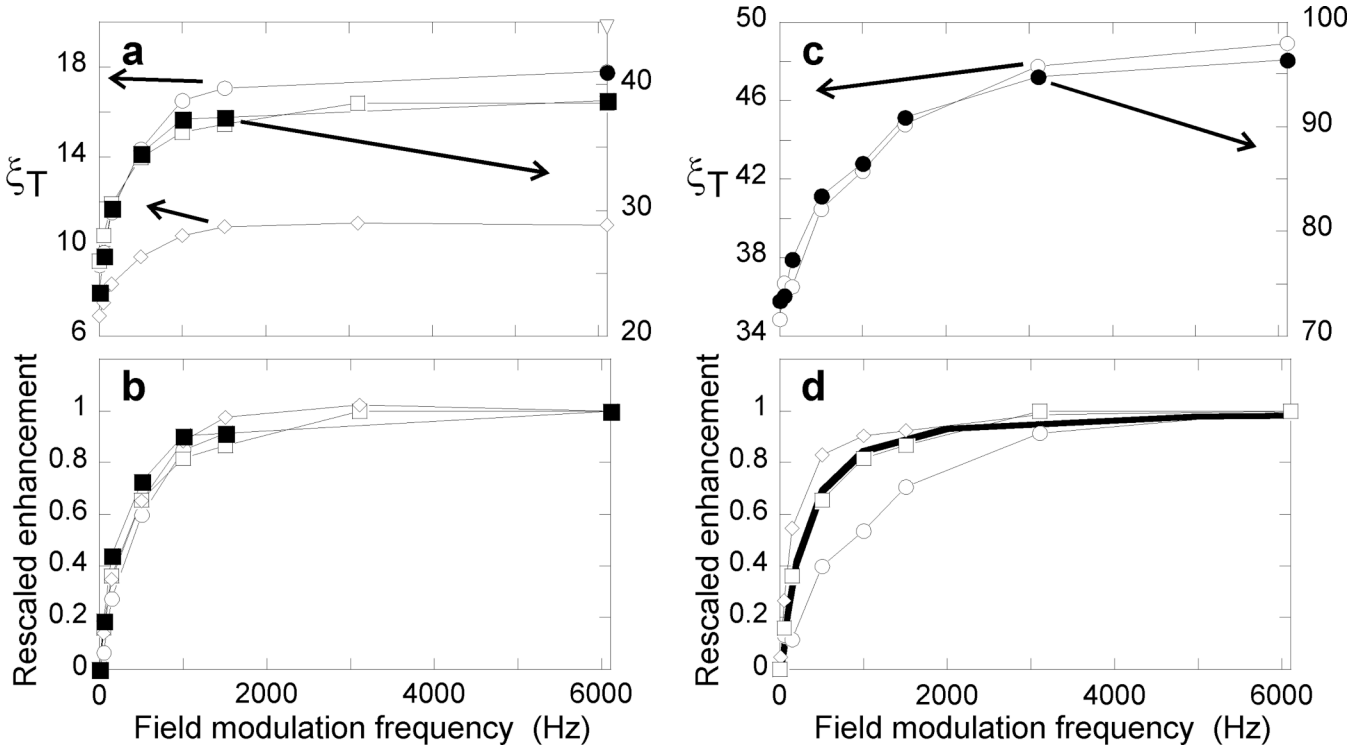

Figure 6.

(a) DNP signal enhancements as a function of field modulation frequency for 20 mM TOTAPOL. Open symbols are at 35 K (left axis); closed symbols are at 16 K (right axis). Rms modulation amplitudes are 40 G (▽), 20 G (○,●), and 10 G (◊,□,■). Microwave power from the source is 30 mW (▽,○,●,□,■) or 12 mW (◊). (b) Same data (○,□,■,◊) rescaled to 0.0 at 0 Hz and 1.0 at 6100 Hz. (c) Same as panel a, but for 20 mM DOTOPA-TEMPO with 30 mW microwave power and 10 G rms field modulation at 35 K (○, left axis) and 16 K (●, right axis). (d) Rescaled DNP signal enhancements for 20 mM DOTOPA-TEMPO (○), 20 mM TOTAPOL (□), and 40 mM 4-amino-TEMPO (◊) at 35 K with 10 G rms field modulation and 30 mW microwave power. Thin lines in all panels are drawn to guide the eye. Thick line in panel d shows the simulated dependence on modulation frequency for 40 mM 4-amino-TEMPO, with no adjustable parameters (see text).

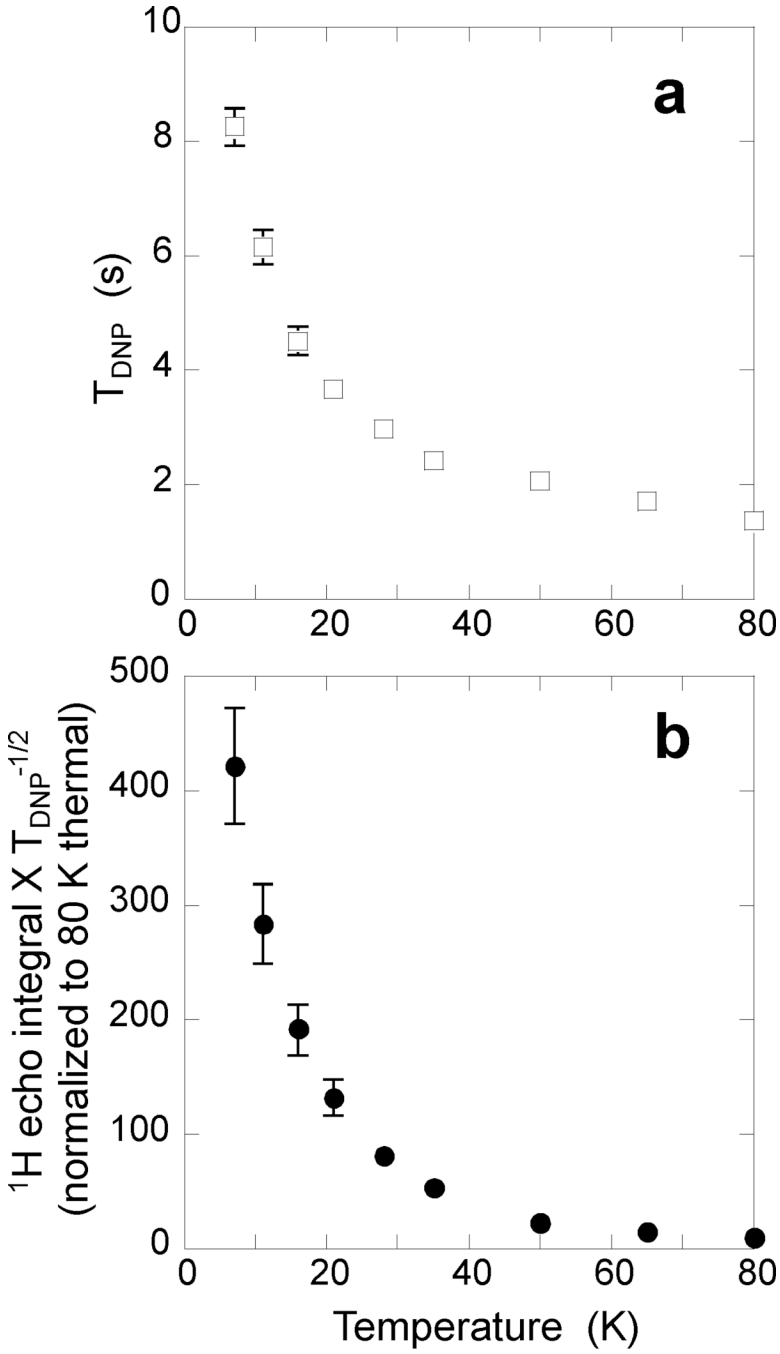

Figure 7.

(a) Temperature dependence of DNP build-up time for 30 mM DOTOPA-TEMPO. (b) Temperature dependence of the DNP-enhanced ^{1}H NMR signal divided by the square-root of T_{DNP}, normalized to the thermal equilibrium signal at 80K divided by the square-root of the ^{1}H spin-lattice relaxation time at 80 K. This plot represents the temperature dependence of the DNP sensitivity enhancement, relative to measurements without DNP at 80 K.

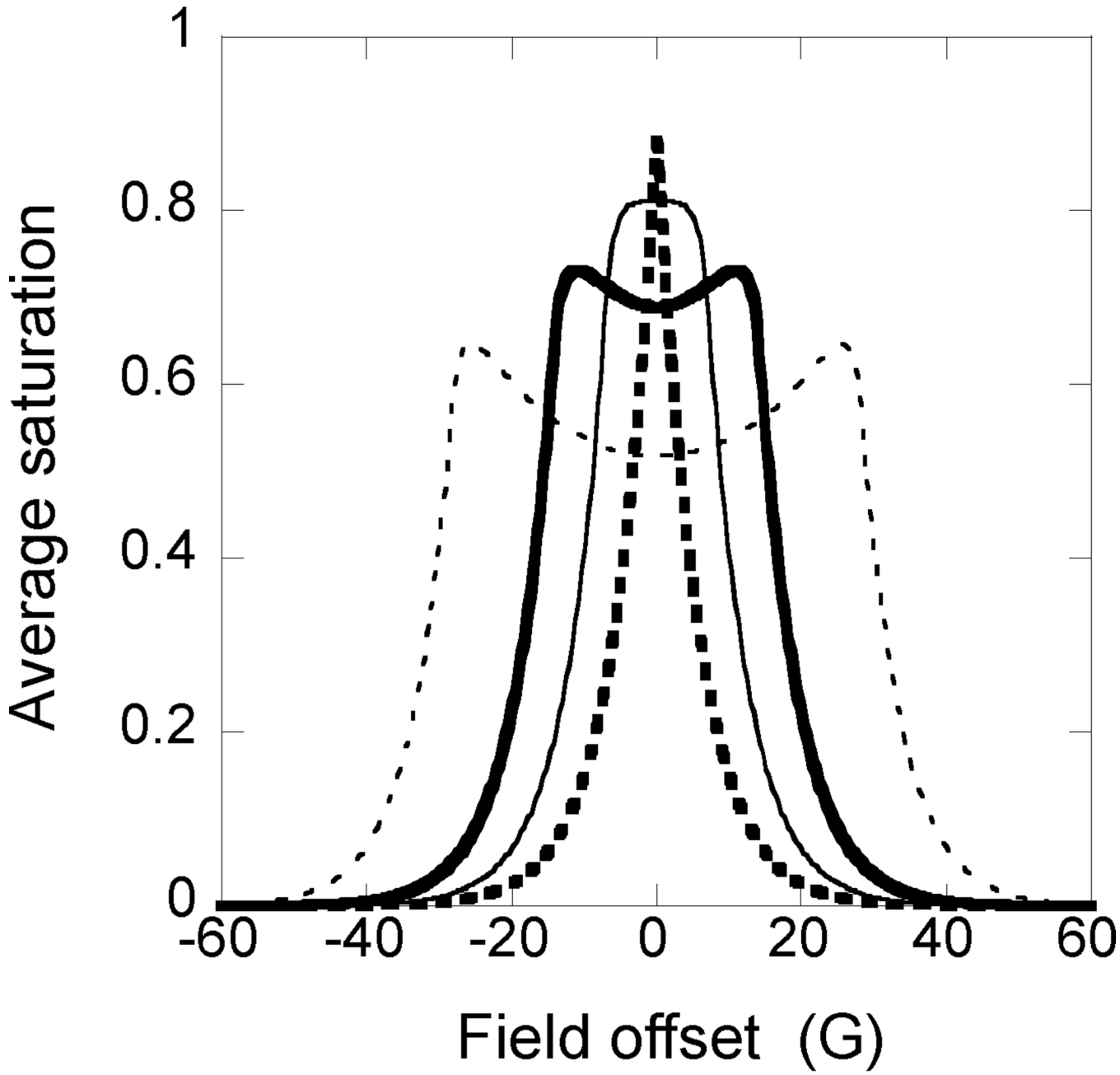

Figure 8.

Simulations of electron spin saturation within an inhomogeneously broadened EPR line for various field modulation amplitudes (0.1 G rms = thick dashed line, 5 G rms = thin solid line, 10 G rms = thick solid line, 20 G rms = thin dashed line). The saturation value is the average over a complete modulation cycle, after equilibration. The simulations assume a 10 kHz modulation frequency, T_{1e} = 2 ms, T_2 = 4 μs, B_1 = 0.03 G, and a spectral diffusion constant of 10^{17} Hz^2/s.

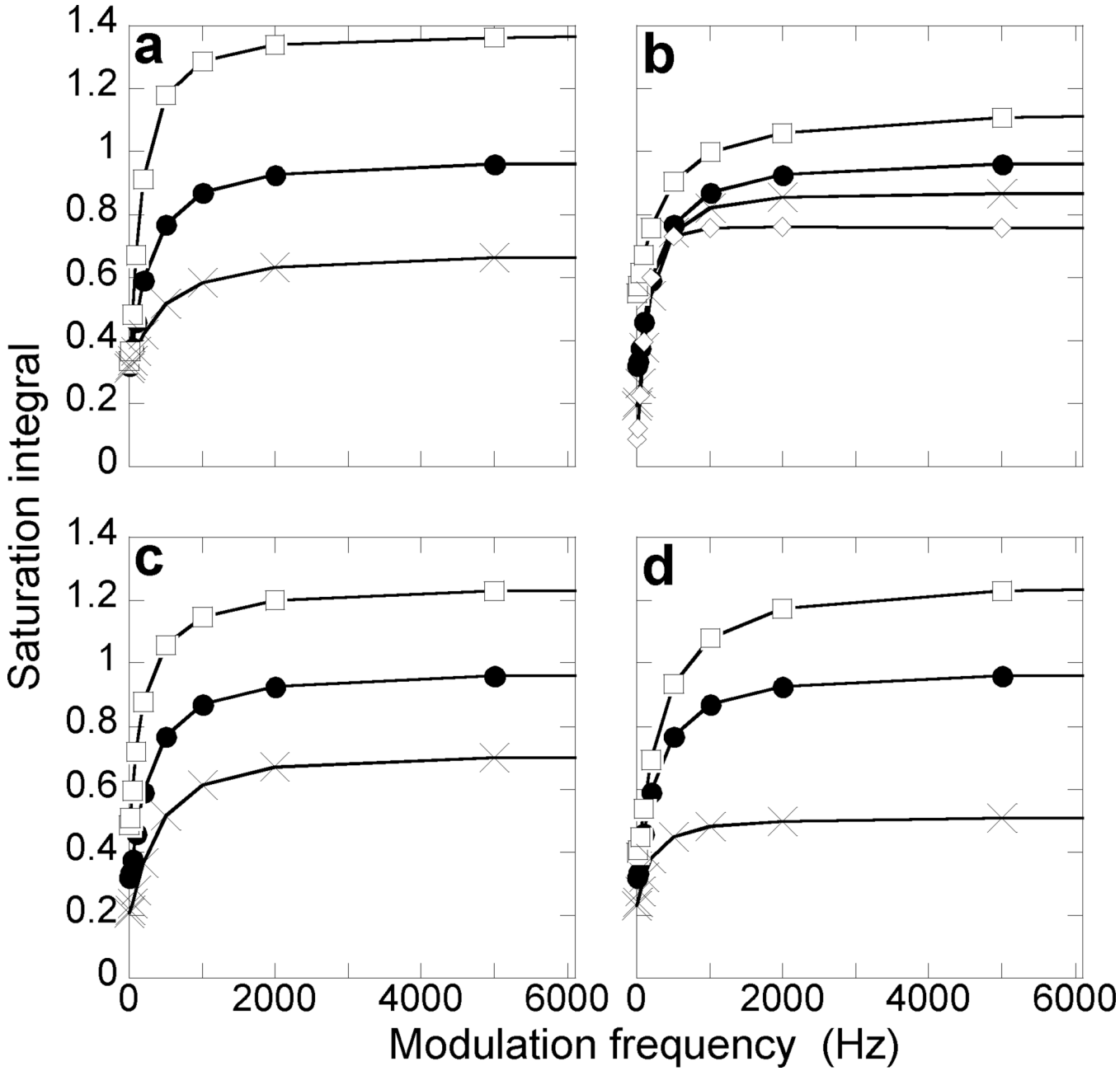

Figure 9.

Simulations of the total electron spin saturation within an inhomogeneously broadened EPR line as a function of the field modulation frequency, with variations in each simulation parameter. (a) Root-mean-squared modulation amplitude equal to 5 G (×), 10 G (●), or 20 G (□). (b) Spectral diffusion constant (Hz^2/s) equal to 0 (◊), 0.3×10^{17} (×), 1×10^{17} (●), or 4×10^{17} (□). (c) T_{1e} equal to 1 ms (×), 2 ms (●), or 4 ms (□). (d) B_1 equal to 0.015 G (x), 0.03 G (●), or 0.06 G (□). When one parameter is varied, the other parameters have the following values: modulation amplitude = 10 G rms, diffusion constant = 1×10^{17} Hz^2/s, T_{1e} = 2 ms, B_1 = 0.03 G, and T_2 = 4 μs. Simulated saturation values are normalized so that complete saturation over a 28 G spectral region (covered by 10 G rms field modulation) corresponds to an integral of 1.0. Lines are drawn to guide the eye.

Table 1

Summary of ^{1}H DNP measurements on glycerol/water with various nitroxide dopants. Uncertainties in DNP signal enhancements are roughly ±30%, estimated from repeated measurements on several samples and attributed to variations in microwave alignment. Uncertainties in T_{DNP} values are ±10% or less, unless otherwise noted.

Temperature (K)	Dopant	Dopant concentration[a] (mM)	DNP Signal enhancement[b]	DNP-enhanced signal[c] (arb. units)	T_{DNP} (s)	DNP-enhanced signal × $(T_{DNP})^{-1/2}$	Ratio of DNP-enhanced signals with and without field modulation[d]
80	DOTOPA-TEMPO	20	12x	18	2.7 ± 0.7	11	n.d.
	DOTOPA-TEMPO	30	10x	17	1.4	14	n.d.
	TOTAPOL	20	6x	12	8.3	4.1	n.d.
	4-amino-TEMPO	40	11x	12	50 ± 15	1.8	n.d.
	4-amino-TEMPO	80	13x	17	7.0	6.5	n.d.
	4-amino-TEMPO	160	15x	9.4	1.2 ± 0.2	8.5	n.d.
	4-amino-TEMPO	320	9x	3.4	<1		n.d.
35	DOTOPA-TEMPO	20	34x	114	5.6	48	1.5
	DOTOPA-TEMPO	30	26x	114	2.4	73	1.2
	TOTAPOL	20	11x	57	18.5	13	1.5
	4-amino-TEMPO	40	13x	33	90 ± 30	3.6	2.4
	4-amino-TEMPO	80	41x	118	14.1	31	n.d.
	4-amino-TEMPO	160	34x	65	2.4	43	1.1
16	DOTOPA-TEMPO	20	75x	578	10.6	177	1.3
	DOTOPA-TEMPO	30	59x	563	4.5	265	n.d.
	TOTAPOL	20	26x	333	41	52	1.5
	4-amino-TEMPO	40	29x	168	126	15	1.7
	4-amino-TEMPO	80	82x	579	27	111	n.d.
	4-amino-TEMPO	160	54x	245	3.4	133	n.d.
	4-amino-TEMPO	320	15x	57	0.8 ± 0.2	63	n.d.
7	DOTOPA-TEMPO	30	81x	1666	8.2	580	1.1
	4-amino-TEMPO	40	48x	232	>200		n.d.

[a] All samples are 10 µl of 25/75 mol% glycerol/water. The 30 mM DOTOPA-TEMPO sample has 0.22 M acetate buffer, pH 3.

[b] Ratio of ^{1}H NMR spin echo integral with DNP to the integral without DNP, for the same sample and temperature, using 30 mW at 264.0 GHz, $\tau = 2T_{DNP}$, and no field modulation. For 40 mM 4-amino-TEMPO, τ = 170 s.

[c] Spin echo integral with DNP, using 30 mW at 264.0 GHz, $\tau = 2T_{DNP}$, and no field modulation. For 40 mM 4-amino-TEMPO, τ = 170 s.

[d] Spin echo integral with DNP, using 30 mW at 264.0 GHz, $\tau = 2T_{DNP}$, and 10 G rms field modulation during τ, with 6 kHz modulation frequency. n.d. = not determined.